A Fast and Easy Way to Produce a 1-Km All-Weather Land Surface Temperature Dataset for China Utilizing More Ground-Based Data

Yanru Yu[ID], Shibo Fang, Wen Zhuo, and Jiahao Han

Abstract— Land surface temperature (Ts) is one of the important parameters of the Earth's surface, but the temporal and spatial incompleteness of Ts data has severely limited its application in many important fields, such as climate change, extreme weather, numerical weather prediction, and agro-meteorological disasters. The MODIS daily Ts data are relatively high temporal and spatial resolution data, but they also have a large amount of missing data due to the influence of clouds or other atmospheric conditions. Gap filling is currently the only means of obtaining complete high spatial and temporal resolution remote sensing Ts data. However, the current gap filling results either fail to guarantee the filling accuracy due to the difficulty of obtaining ground observation data or fail to generalize the gap filling method over a large area due to its inefficiency. In this study, we first obtained the daily mean Ts (dmTs) data under MODIS clear-sky condition using multiple linear regression based on Ts data from nearly 2400 meteorological observation stations and then proposed a new method to fill Ts in the cloudy-sky condition. The validation with in situ data showed that the precision of filled Ts in clear-sky condition indicates that its root-mean-square error (RMSE) is between 1.52–2.36 K, and in cloud-sky condition, its RMSE is 2.73 K. It is confirmed that the method has the advantages of efficiency, simplicity, and accuracy and is the most suitable method for filling Ts data at national and continental levels. The all-weather 1-km dmTs data reconstructed in this study are of great value on urban heat island intensity studying, air temperature generating, drought monitoring, and other associated applications.

Index Terms— Gap filling, land surface temperature, reconstruction, remote sensing.

I. INTRODUCTION

LAND surface temperature (Ts) is a critical variable in various research fields, such as urban heat island, extreme weather, drought monitoring, and climate change [1], [2], [3], [4], [5]. Currently, accurate Ts data are primarily obtained from real-time observations at a limited number of meteorological stations. However, these stations are widely distributed spatially, leading to the increasing popularity of

using satellite remote sensing data. Despite some limitations, such as cloud contamination or other atmospheric conditions, this can result in missing Ts data [6], [7], [8], [9].

The production of Ts data from satellites can be divided into two categories. One category includes Ts data with very high temporal resolution (1 h or finer) but coarse spatial resolution (2)–5 km), obtained from geostationary satellites such as Geostationary Operational Environmental Satellite (GOES) [10], the Spinning Enhanced Visible and Infrared Imager onboard Meteosat Second Generation (MSG-SEVIRI). [11], and Himawari-8 Advanced Himawari Imager (AHI) [12], [13]. The other category consists of Ts data with high-to-moderate spatial resolution (100 m–1 km) but a relatively long revisiting period (1)–16 days), obtained from polar-orbiting satellites, such as Landsat and Advanced Spaceborne Thermal Emission and Reflection Radiometer (ASTER) [14], [15], Advanced Very High-Resolution Radiometer (AVHRR) [16], and Moderate Resolution Imaging Spectroradiometer (MODIS) [17], [18].

The incompleteness and low spatial resolution of the data are the two most critical issues limiting the application of Ts data. Gap filling of polar-orbiting satellite data with high spatial resolution is the mainstream way to solve the above problems. The filling methods can be categorized into two types. One type is to fill the Ts in clear sky [19], [20], [21], mostly done by interpolation, which can be categorized into temporal interpolation, spatial interpolation, and hybrid temporal and spatial interpolation. Most of the temporal interpolation methods are based on periodic variations of Ts, e.g., diurnal temperature cycle (DTC) model [22], annual temperature cycle (ATC) model [23], [24], [25], harmonic analysis of time series (HANTS) [26], Savitzky–Golay (S–G) filtering [27], [28], and Fourier transforms [29]. As for spatial interpolation methods, most of them are geostatistical interpolation based on existing valid data, including inverse distance weighted interpolation [30], [31], kriging interpolation [32], [33], spline interpolation [34], geographically weighted regression [20], and their variants. Hybrid methods mostly combine temporal and spatial interpolation methods [35], [36]. Various methods have obtained complete monthly Ts, eight-day Ts, and even daily Ts with the valid clear-sky data, but the reconstructed results tend to be higher than the real Ts value and may not accurately reflect the true state of the land surface. This is because the presence of clouds reduces the solar radiation

TABLE I
DATA USED IN THIS STUDY

Data	Spatial resolution	Temporal resolution	Source	Time period	Spatial extent
Terra Ts	1 km	1 day	https://ladsweb.modaps.eosdis.nasa.gov/search/	2011-2020	China land
Aqua Ts	1 km	1 day	https://ladsweb.modaps.eosdis.nasa.gov/search/	2011-2020	China land
Insitu Ts	2388 Sites	1 hour/day	http://data.cma.cn/	2011-2020	China land
Elevation	30 arcsecond	No	http://earthexplorer.usgs.gov	No	China land
ERA5-land Ts	0.1°	1 day	https://cds.climate.copernicus.eu/cdsapp#!/dataset/reanalysis-era5-land	2011-2020	China land

received by the ground, making the actual Ts lower than that of the clear-sky condition.

The other category is to fill the Ts for cloudy sky [37], [38], [39], which is mostly done by fusing other data, like with passive microwave remote sensing Ts data [40], [41], [42], geosynchronous geostationary satellite data [38], surface energy balance [37], [43], [44], and reanalysis data [45]. The methods of filling Ts data under cloudy-sky conditions can be categorized into three groups. The first involves directly filling the missing regions with other Ts data, such as passive microwave Ts data [46] or reanalysis data. However, this approach may reduce the accuracy of the final filled Ts due to differences in data resolution. The second category involves combining other auxiliary variables, such as elevation data, vegetation indices, radiation data, and air temperature data, to fill Ts by constructing relational models. Model construction methods include linear regression [41], [47], machine learning [48], [49], [50], and deep learning. The third category involves filling Ts using land surface energy equations [51]. The process of reconstructing cloud-sky Ts is generally complex. In addition to differences in spatial and temporal resolution between different data sources, the uncertainties of the auxiliary variables themselves will also affect the results. Moreover, a higher computational power is required due to the inclusion of more auxiliary data.

Ground-truth Ts data are the standard for measuring the accuracy of filled Ts data. Due to the limited number of stations, researchers typically use it for validation purposes and rarely incorporate it into the reconstructed results. However, by including a sufficient quantity of ground-truth data with good quality assurance, the accuracy of reconstructed Ts can be significantly improved. Therefore, in this study, high-quality ground-truth Ts data from 2388 stations out of nearly 10 000 observation sites in China were carefully selected after quality control to contribute to the reconstruction of daily mean Ts (dmTs) data.

Overall, the main objective of this study is to achieve the simple and rapid acquisition of high-precision all-weather high temporal and spatial resolution dmTs data. Initially, a multiple linear regression method was utilized to establish the relationship between instantaneous Ts and dmTs from ground observation in order to obtain the satellite dmTs data

in the clear-sky region. Subsequently, the proposed method was compared with two other methods for filling cloudy-sky Ts. Finally, the filled results were validated and the dynamics of the dmTs in China within the period of 2011–2020 were analyzed.

II. DATA

The data used in this work are listed in Table I. The MOD11A1 and MYD11A1 daily Ts products are the base data for estimating dmTs in this study. The MODIS sensor is mounted on the Terra and Aqua satellites, which provide four observations of the Earth per day, at local times of 1:30, 10:30, 13:30, and 22:30. The MOD11A1 and MYD11A1 products provide 1-km daily Ts and emissivity data with the generalized split-window algorithm [52]. The daily Ts products from 2011 to 2020 were used in the present study for the all-weather dmTs reconstruction, which can be downloaded from the National Aerodynamics and Space Administration (NASA) website (https://search.earthdata.nasa.gov).

The ground-based dmTs and hourly Ts were obtained from the China Meteorological Information Center (CMIC), which were used as important auxiliary and reference data for the reconstruction of all-weather MODIS dmTs. Fig. 1 displays the geographical location of the 2388 meteorological observation stations.

The ERA5-land dmTs datasets were also used in this study for cloudy-sky Ts data filling. The ERA5-land data are the global dataset produced by the European Centre for Medium-Range Weather Forecasts (ECMWF) through the enhancement of the land component of the fifth generation of the European Reanalysis (ERA5), referred to as ERA5-land. Differences between ERA5-land Ts data and MODIS Ts data were evaluated to be minimal [53], so we selected ERA5-land Ts data to fill in the missing parts of the MODIS Ts data. The nearest neighbor resampling method was used to unify the resolution of ERA5 Ts data to the same as the MODIS Ts data.

III. METHODOLOGY

The reconstruction of all-weather dmTs is categorized into clear-sky and cloudy-sky conditions. We define the clear-sky
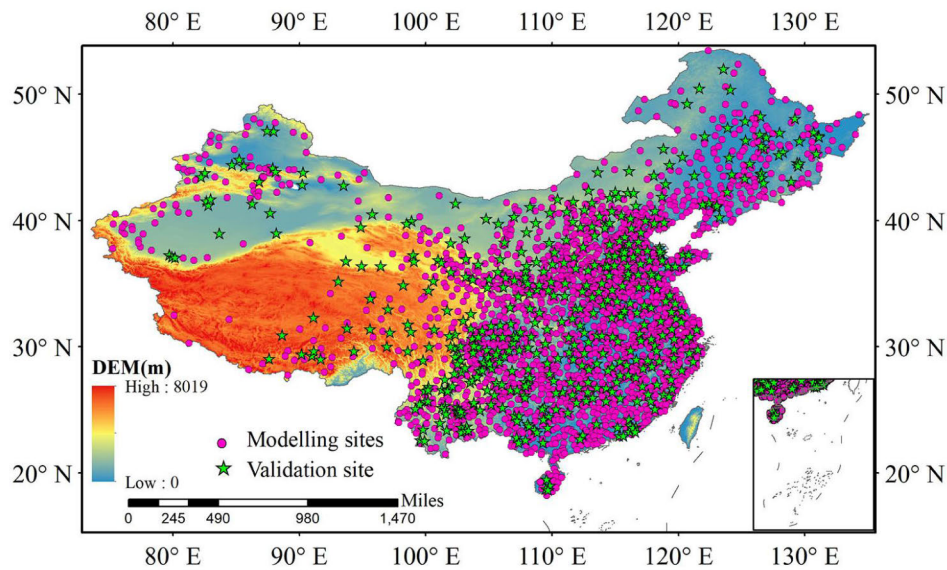
Fig. 1. Spatial distribution map of meteorological stations, with pink dots representing the stations used for modeling and green pentagrams representing the stations used for validation. The background image shows the surface elevation.
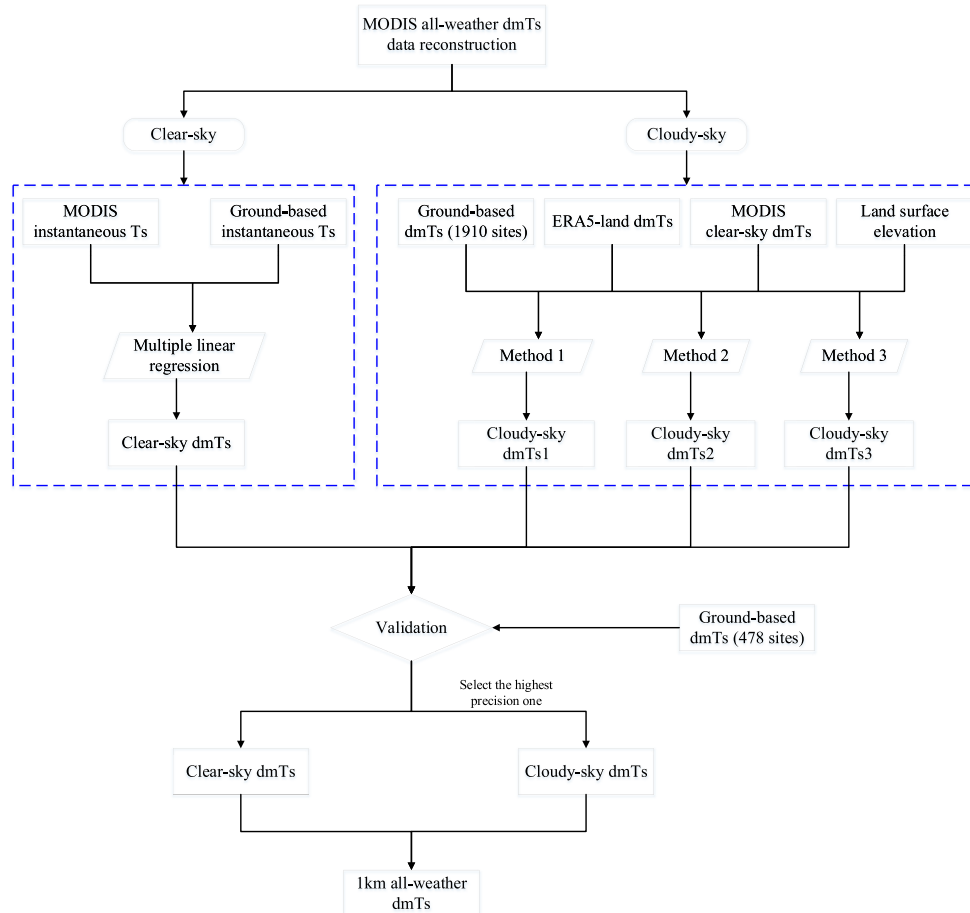

Fig. 2. Summary flowchart for reconstructing MODIS all-weather dmTs data.

condition as having at least one valid daytime Ts and one valid nighttime Ts in the four instantaneous daily Ts data from MODIS and vice versa for the cloudy-sky condition. Generally, the MODIS dmTs was obtained by averaging all the clear-sky instantaneous Ts or the maximum and minimum values in a day. However, since MODIS has only four observations per day, the averaging of the instantaneous values is not sufficient to represent the daily mean state [54].
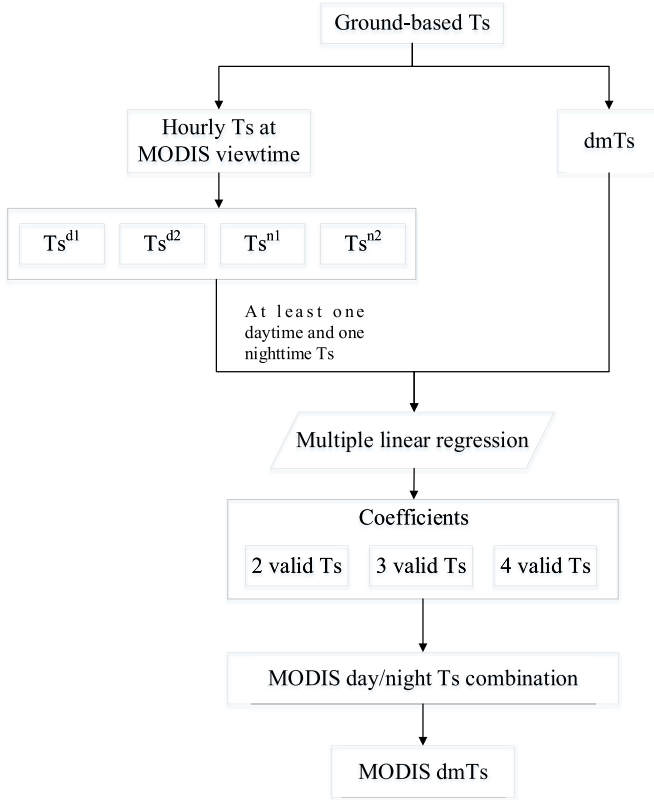
Fig. 3. Framework for reconstruction of clear-sky Ts. Ts^{d1}, Ts^{d2}, Ts^{n1}, and Ts^{n2} are the values of in situ Ts at the four MODIS observation time of Terra daytime, Aqua daytime, Terra nighttime, and Aqua nighttime, respectively.

Thus, for the clear-sky condition, multiple linear regression (MLR) method was applied instead of averaging to estimate the more accurate dmTs. While the reconstruction of dmTs under cloudy-sky conditions was a concern, we compared the proposed method with two other methods to achieve higher accuracy in obtaining the dmTs data. The overall study scheme is illustrated in Fig. 2, and a detailed description of the reconstruction method for clear-sky and cloudy-sky dmTs is provided as follows.

A. Reconstruction of Clear-Sky Ts

The main idea of this section is to obtain MODIS dmTs data by the quantitative relationship between ground observed instantaneous and dmTs. Xing et al. [47] believe that there is the same quantitative relationship between the instantaneous Ts and the dmTs at the same moments from both in situ and satellite observations and verified the idea in the global scale with 0.05° spatial resolution. Therefore, we migrated this idea to the Chinese regional 1-km data for the reconstruction of MODIS all-weather dmTs data. The clear-sky dmTs reconstruction mainly consists of two parts: in situ Ts relationship construction and satellite dmTs estimation with the in situ Ts relationship coefficients. The flow is shown in Fig. 3.

To construct an accurate quantitative relationship between instantaneous and dmTs applicable to satellites, obtaining in situ observational data at the moment of satellite observation is the first step. However, the acquisition time of the

ground measurement Ts does not exactly match the satellite observation time, so the ground observation Ts at the satellite observation times is first obtained by linear interpolation based on the assumption that the Ts varies in a linear manner within a short period of time. Next, multiple linear regression methods were used to obtain the coefficients between the in situ instantaneous Ts and the dmTs. Since the satellite provides observation data at four moments per day, there can be nine combinations under the principle of guaranteeing at least one valid daytime Ts and one valid nighttime Ts. In situ Ts from 1910 sites (80% of the total number of sites) for the period 2011–2020 were used for coefficient determination. The combination of regression models used in this study is as follows.

Combination With 2 Valid Ts:

$$dmTs = k_1 \times Ts^{d1} + k_2 \times Ts^{n1} + \varepsilon$$
$$dmTs = k_1 \times Ts^{d1} + k_2 \times Ts^{n2} + \varepsilon$$
$$dmTs = k_1 \times Ts^{d2} + k_2 \times Ts^{n1} + \varepsilon$$
$$dmTs = k_1 \times Ts^{d2} + k_2 \times Ts^{n2} + \varepsilon. \tag{1}$$

Combination With 3 Valid Ts:

$$dmTs = k_1 \times Ts^{d1} + k_2 \times Ts^{d2} + k_3 \times Ts^{n1} + \varepsilon$$
$$dmTs = k_1 \times Ts^{d1} + k_2 \times Ts^{d2} + k_3 \times Ts^{n2} + \varepsilon$$
$$dmTs = k_1 \times Ts^{d1} + k_2 \times Ts^{n1} + k_3 \times Ts^{n2} + \varepsilon$$
$$dmTs = k_1 \times Ts^{d2} + k_2 \times Ts^{n1} + k_3 \times Ts^{n2} + \varepsilon. \tag{2}$$

Combination With 4 Valid Ts:

$$dmTs = k_1 \times Ts^{d1} + k_2 \times Ts^{d2} + k_3 \times Ts^{n1} + k_4 \times Ts^{n2} + \varepsilon. \tag{3}$$

For (1)–(3), the dmTs is the in situ daily mean land surface temperature and k_i and ε are the model coefficients. $d1$, $d2$, $n1$, and $n2$ represent MODIS observation times for Terra daytime, Aqua daytime, Terra nighttime, and Aqua nighttime, respectively.

The estimation of MODIS dmTs is based on the fitting coefficients of (1)–(3) corresponding to different combinations after screening MODIS daytime and nighttime valid observations.

B. Reconstruction of Cloudy-Sky Ts

In order to improve the data reconstruction accuracy, MODIS Ts grid data with invalid values matched with 1910 meteorological stations were filled with in situ Ts data at the same time. For the invalid pixels without meteorological stations, the study proposes a temperature difference (TD) correction method to fill them and compares it with two other cloudy-sky filling methods (linear correction method and elevation temperature gradient regression method). The methods are described in detail as follows.

1) Temperature Difference Correction Method (TDCM): The TDCM method reconstructs dmTs data under cloudy-sky by correcting ERA5-land dmTs with MODIS clear-sky dmTs and in situ dmTs. The corrected way is based on the difference between ERA5-land dmTs and the merged dmTs by MODIS
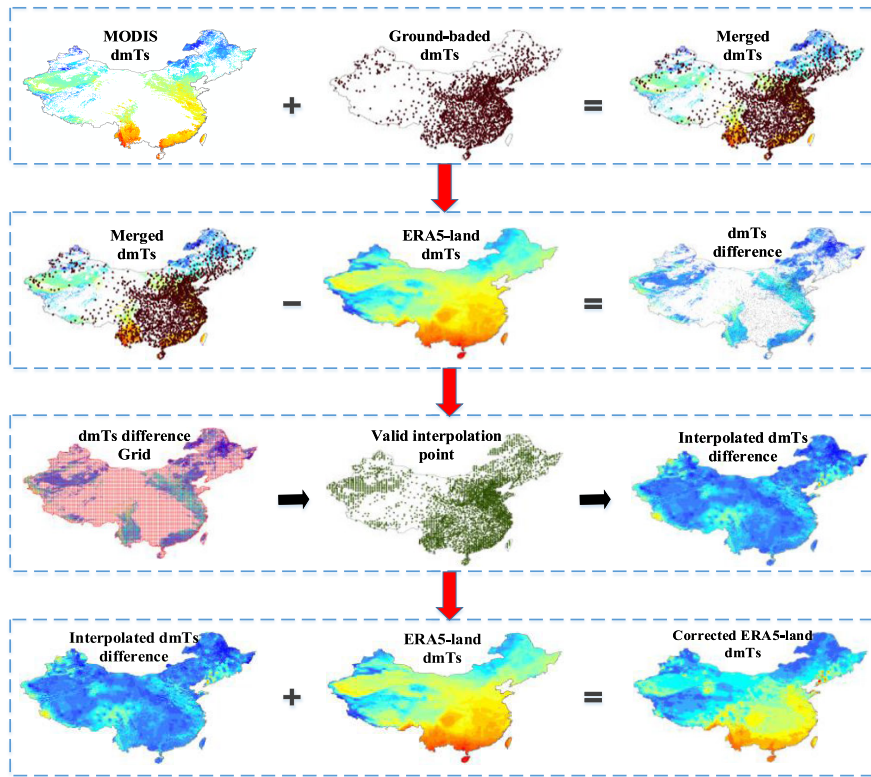
Fig. 4.   Flowchart of the TDCM method.

and in situ. We consider the TD between merged dmTs and ERA5-land dmTs to be similar among neighboring pixels at the same time. The TDCM is divided into four steps, as shown in Fig. 4.

Step 1: Merge MODIS dmTs and in situ dmTs from 1910 meteorological observation stations.

Step 2: Calculate the TD between the merged dmTs and ERA5-land dmTs.

Step 3: In order to obtain a larger number and a more uniform distribution of interpolation points, the TD was divided into a 100×100 grid and the mean value of the valid data within each grid was calculated as the interpolation point, followed by IDW interpolation to obtain the pixel-by-pixel TD data.

Step 4: Calculate the sum of ERA5-land dmTs and interpolated TD to obtain the filled dmTs data.

2) Linear Correction Method (LCM): The basic idea of the LCM is to correct the ERA5-land dmTs data based on the dmTs data from meteorological observation stations. First, the dmTs data of 1910 meteorological observation stations from 2011 to 2020 are used to perform a linear regression with the dmTs data of ERA5-land at the same locations and times to obtain the regression coefficients. Then, the regression coefficients are interpolated to the grid data by using the inverse distance weighting (IDW) method [55]. Finally, the grid correction coefficients are used to correct the ERA5-land dmTs data. The flow is shown in Fig. 5.

The linear correction equation is expressed as

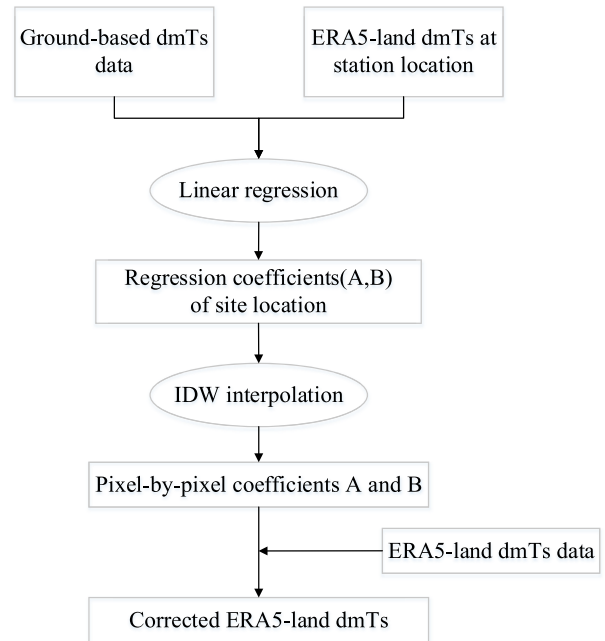$$\text{CdmTs} = A \times \text{dmTs}^{\text{ERA5}} + B \qquad (4)$$

Fig. 5.   Flowchart of LCM method.

where CdmTs is the dmTs reconstructed by linear correction method. The coefficients A and B are the slope and intercept of the linear regression, respectively.

3) Elevation Temperature Gradient Regression Method (ETGRM): A close relationship exists between Ts and surface elevation, so it is feasible to utilize the gradient change characteristics between surface elevation and Ts to reconstruct
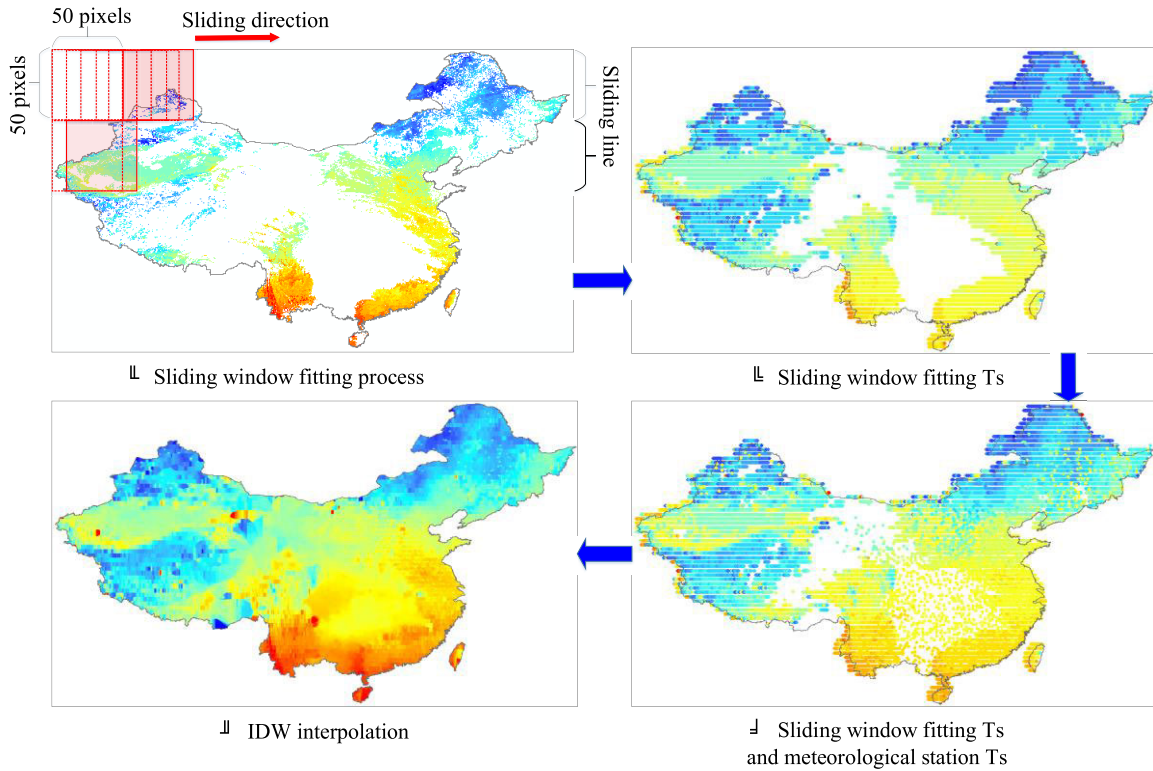
Fig. 6. Flowchart of ETGRM reconstruction of cloudy-sky Ts.

seamless Ts data. To improve the filling accuracy of invalid pixels, the ETGRM was implemented within a selected window size in this study. Window sizes of 20 × 20 pixels, 50 × 50 pixels, 80 × 80 pixels, 100 × 100 pixels, 150 × 150 pixels, and 200 × 200 pixels were performed for the experiments, and it was found that the error is minimized and enough to reflect the spatial heterogeneity of the land surface temperature when the size of the sliding window is 50 × 50 pixels.

Specifically, the ETGRM process consists of four steps (see Fig. 6). First, a linear regression relationship between DEM and dmLST is established within a sliding window size. Second, the Ts values of the fit points were obtained based on the ETGRM fitting coefficients. Third, Ts values for 1910 weather station locations were added to increase the total number and the uniformity of the spatial distribution of interpolated points. Finally, IDW interpolation is performed.

C. Accuracy Verification of Reconstruction

To validate the accuracy of the Ts reconstruction method used in this study, we divided the 2388 ground observations into two groups. The first group (1910 sites) is 80% of sites from 2011 to 2020, which is used to reconstruct the clear-sky and cloudy-sky conditions dmTs. The second group (478 sites) is 20% of sites from 2011 to 2020, which is used to validate the accuracy of reconstruction results. The validation sites are evenly distributed across different surface elevation ranges and are able to represent the status of different land cover types within different climate zones (see Fig. 1). The root-mean-square error (RMSE) and

coefficient of determination (R^2) are used as measures of accuracy.

D. Trend Analysis of dmTs Time Series

In this study, we analyzed the trends of the in situ Ts and filled dmTs with Mann–Kendall test and Theil–Sen slope. The Mann–Kendall test is a nonparametric test suitable for detecting the warming/cooling trends of Ts time series and quantifying the significance level of Ts time series [56], [57]. The Theil–Sen slope is equipped with the ability to reduce the effect of outliers in the Ts time series [58], [59]. We conducted the Mann–Kendall test for both in situ and filled dmTs data and compared their Theil–Sen slopes in describing Chinese dmTs trends.

IV. RESULTS

A. Reconstruction of Clear-Sky dmTs

Fig. 7 shows the scatter plots for daily mean in situ observations Ts against the dmTs estimated by (1)–(3) of the multiple linear regression method. Table II displays the coefficients and the accuracy indicators of the regression. The result shows that the dmTs obtained from the multiple linear regression is very close to the dmTs measured at the meteorological observation stations, with R^2 ranges from 0.97 to 0.99 and the RMSE ranges from 1.47 to 2.24 K. In general, the more valid observations, the higher the Ts accuracy of the fit. This is confirmed by our results, in which the average RMSE is 1.87 K for the combination of two valid observations, 1.65 K for the combination of three valid
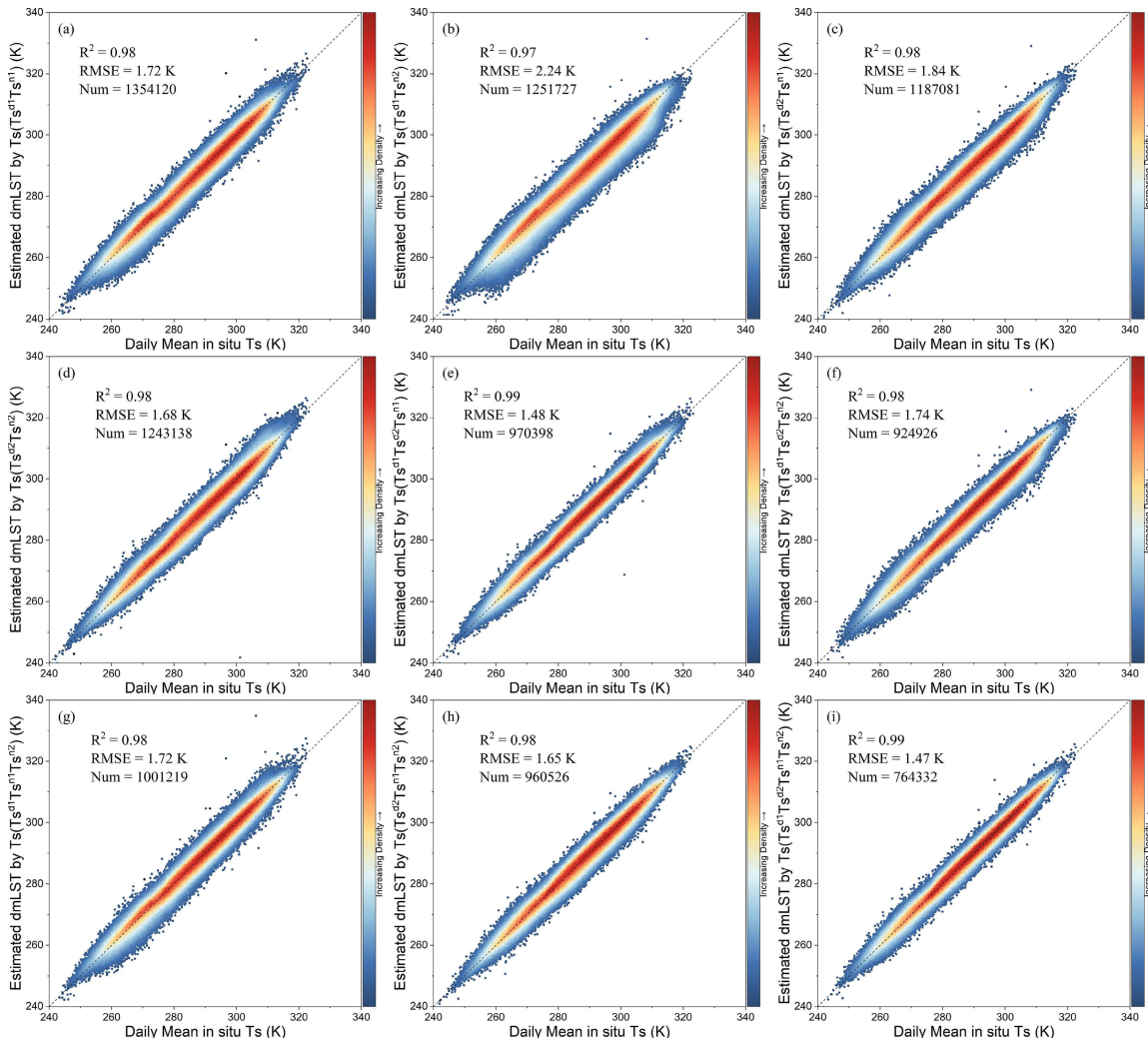
Fig. 7. Scatter plots of daily mean in situ Ts versus daily mean Ts estimated with multiple linear regression using (1)–(3) at 1910 meteorological stations from 2011 to 2020. The gray diagonal lines are 1:1 lines. (a)–(i) dmTs estimated with the combinations of $Ts^{d1}\_Ts^{n1}$, $Ts^{d1}\_Ts^{n2}$, $Ts^{d2}\_Ts^{n1}$, $Ts^{d2}\_Ts^{n2}$, $Ts^{d1}\_Ts^{d2}\_Ts^{n1}$, $Ts^{d1}\_Ts^{d2}\_Ts^{n2}$, $Ts^{d1}\_Ts^{n1}\_Ts^{n2}$, $Ts^{d2}\_Ts^{n1}\_Ts^{n2}$, and $Ts^{d1}\_Ts^{d2}\_Ts^{n1}\_Ts^{n2}$ versus in situ dmTs.

observations, and 1.47 K for the combination of four valid observations.

As can be seen from Fig. 7 and Table II, the combination Tsd1_Tsn2 (Terra daytime and Aqua nighttime) has the lowest fitting accuracy relative to the other eight combinations, with an R^2 of 0.97 and an RMSE of 2.24 K. The reason for this may be due to the fact that the time interval between the two observation times is relatively short, about 9 h and is not sufficiently representing the average temperature for the whole day.

B. Reconstruction of Cloudy-Sky dmTs

Although the MODIS dmTs estimation method described above improves the amount of valid data and accuracy to a large extent, there is still a large amount of missing data because the thermal infrared sensors are heavily obscured by clouds. Fig. 8 illustrates the amount of data after MODIS clear-sky dmTs reconstructed for each year. As shown, the multiyear average coverage of dmTs is 49%. The highest coverage was in 2014 at about 56% and the lowest was in 2012 at only 45.6%. In conclusion, cloudy-sky dmTs reconstruction is essential as a large amount of data remains missing.
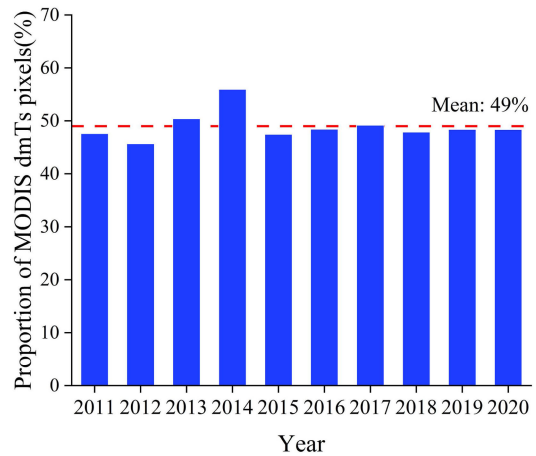

Fig. 8. Proportion of MODIS dmTs pixels for each year 2011–2020.

1) Reconstruction of Cloudy-Sky dmTs With TDCM: In order to improve the accuracy of the dmTs filling, the TDCM process has joined the in situ data, i.e., the value of dmTs corresponding to the meteorological station location is replaced by the in situ data. As a result, the dmTs data corrected by TDCM have values at 1910 site locations that

Combinations	k_1	k_2	k_3	k_4	ε	R^2	RMSE	Number
$Ts^{d1}\_Ts^{n1}$	0.288	0.731	0	0	-3.862	0.98	1.72	1354118
$Ts^{d1}\_Ts^{n2}$	0.342	0.685	0	0	-5.141	0.97	2.24	1251727
$Ts^{d2}\_Ts^{n1}$	0.341	0.682	0	0	-6.291	0.98	1.84	1187081
$Ts^{d2}\_Ts^{n2}$	0.28	0.732	0	0	-3.582	0.98	1.68	1243138
$Ts^{d1}\_Ts^{d2}\_Ts^{n1}$	0.157	0.164	0.69	0	-3.189	0.99	1.48	970398
$Ts^{d1}\_Ts^{d2}\_Ts^{n2}$	0.111	0.26	0.653	0	-6.907	0.98	1.74	924926
$Ts^{d1}\_Ts^{n1}\_Ts^{n2}$	0.843	-0.113	0.285	0	-3.185	0.98	1.72	1001219
$Ts^{d2}\_Ts^{n1}\_Ts^{n2}$	0.506	0.222	0.292	0	-5.443	0.98	1.65	960526
$Ts^{d1}\_Ts^{d2}\_Ts^{n1}\_Ts^{n2}$	0.147	0.587	0.177	0.105	-4.49	0.99	1.47	764332

Note: k1, k2, k3, k4 and ε are the model coefficients, R2 is the goodness-of-fit, RMSE is the root mean square error, and number is the amount of points involved in model fitting.
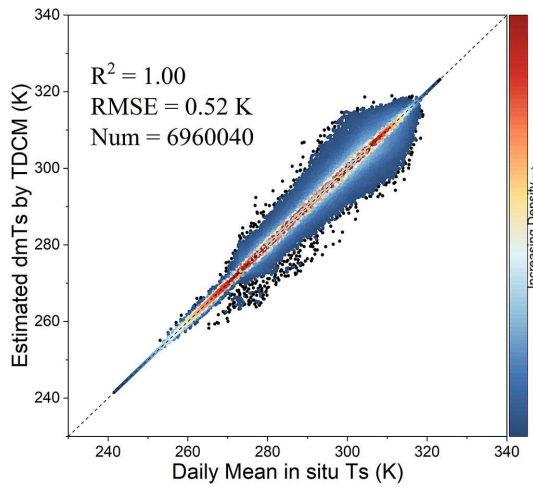

Fig. 9. Scatterplot of dmTs estimated by TDCM versus in situ Ts at 1910 meteorological stations from 2011 to 2020. The gray diagonal lines are 1:1 lines.

agree well with the in situ data, in which R^2 is 1.00 and RMSE is 0.52 K. As shown in Fig. 9, the accuracy of the TDCM reconstructed cloud-sky dmTs is poorer in the high-temperature region ($>$300 K) compared to the low-temperature region ($<$300 K). The reason is that more rainy and cloudy weather in the high-temperature region of southern China, and the serious lack of MODIS Ts data affects the amount of TD data between MODIS and ERA5, which in turn influences the accuracy of the results.

It is also evident from the comparison plots of the selected sample sites in Fig. 10 that the TDCM corrected ERA5 dmTs is in agreement with the dmTs of the meteorological observation stations. Anomalies occur only at very few moments, which are generated during the interpolation process of producing TD data from point to grid. Also, the bias is negligible for the data at the test station locations.

2) Reconstruction of Cloudy-Sky dmTs With LCM: Fig. 11 shows a scatter plot of ERA5-land Ts data before and after corrected by the dmTs data from 2011 to 2020 of 1910 meteorological stations with the regression of LCM against the in situ Ts of meteorological stations. The accuracy of the correction to ERA5-land Ts from meteorological station data is plausible, with an R^2 of 0.95 and an RMSE of 2.70 K.
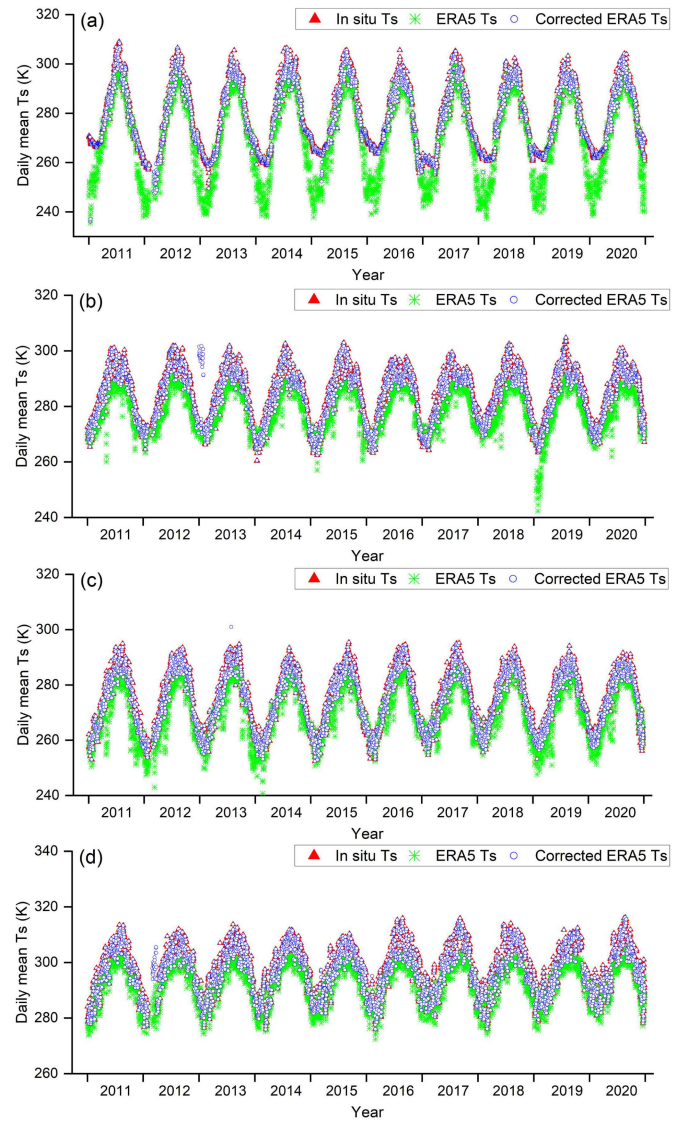

Fig. 10. In situ dmTs, ERA5 dmTs, and corrected ERA5 dmTs by TDCM from 2011 to 2020 of the four randomly selected sites. (a) 50137, (b) 55680, (c) 56004, and (d) 59090.

Compared to the original ERA5-land Ts, the R^2 improves by 0.11, and the RMSE is reduced by 2.23 K.
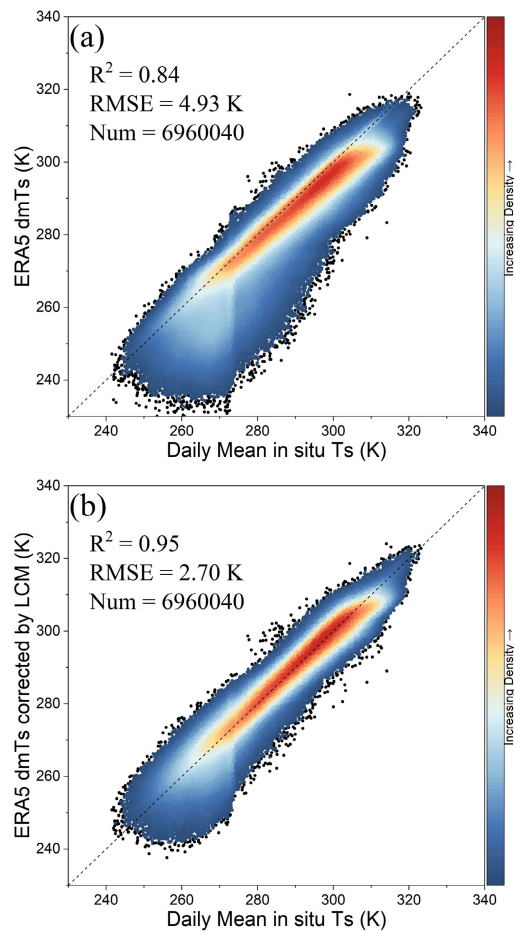
Fig. 11. Scatterplot of ERA5-land dmTs versus in situ Ts before (a) and after (b) corrected by LCM at 1910 meteorological stations from 2011 to 2020. The gray diagonal lines are 1:1 lines.

In terms of time series, as shown in Fig. 12, the in situ dmTs, ERA5-land dmTs, and corrected ERA5-land dmTs from 2011 to 2020 of the four randomly selected sites are shown. It can be seen that the ERA5-land dmTs is overall lower than the in situ Ts by about 0–20 K, while the LCM corrected ERA5 dmTs data significantly narrow the gap with the in situ observations, all within 4 K.

3) Reconstruction of Cloudy-Sky dmTs With ETGRM: The ETGRM cloudy-sky dmTs reconstruction method utilizes the available clear-sky MODIS dmTs and in situ dmTs data within the sliding window to build a quantitative relationship with surface elevation for the reconstruction of the missing dmTs data within the sliding window. Fig. 13 shows the scatter diagrams relating meteorological station data and the data estimated with ETGRM from 2011 to 2020. It can be seen that the deviation of some points leads to a more discrete distribution, but the values of R^2 and RMSE are satisfied with 0.99 and 1.47 K, respectively.

The ETGRM dmTs at the selected four sites is shown in Fig. 14. It can be seen that the ETGRM dmTs of each site is highly compatible with the in situ Ts data. It is because within each sliding window, the data from the station dominate the fitting process due to its continuity in time and sufficient amount of data so that the reconstructed data are more similar to the observatory data at the site location.
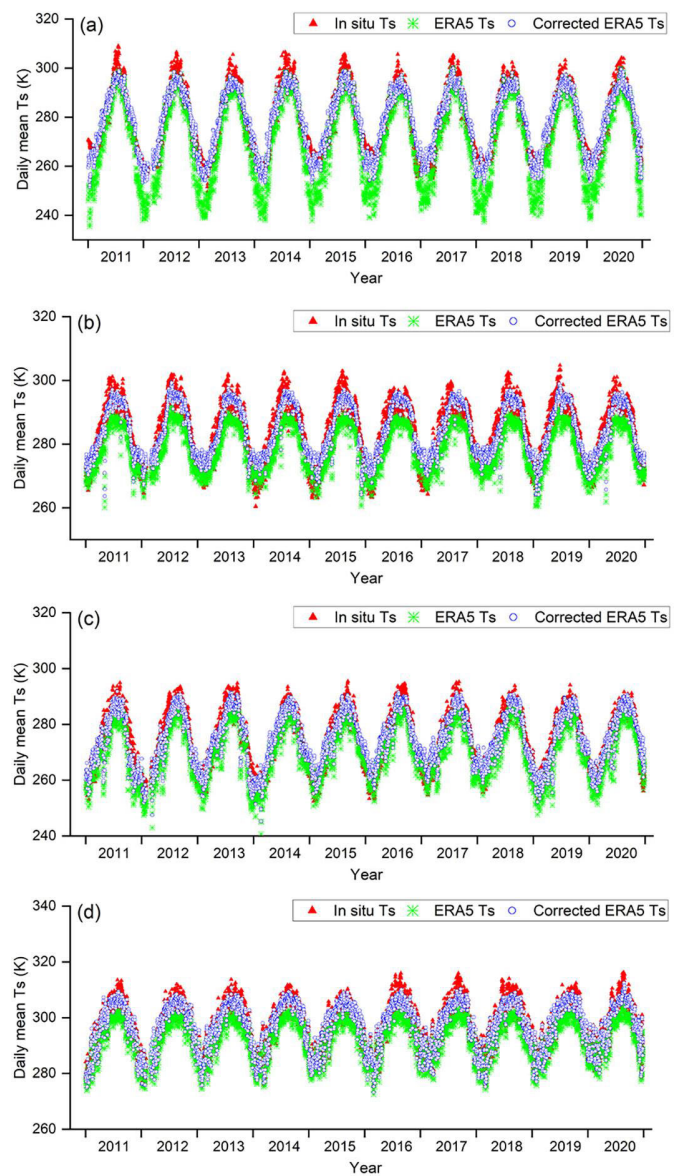

Fig. 12. In situ dmTs, ERA5 dmTs, and corrected ERA5 dmTs by LCM from 2011 to 2020 of the four randomly selected sites. (a) 50137, (b) 55680, (c) 56004, and (d) 59090.

C. Validation of dmTs

The in situ measurements of 478 sites (20% of 2388 sites) were used to validate the result of dmTs reconstruction. Fig. 15(a)–(i) shows the density scatter plots of the daily mean in situ Ts versus the MODIS dmTs estimated by the multiple linear regression method with (1)–(3) at 478 sites from 2011 to 2020. The performance of the validation results was similar to that of the experimental sites, where the multiple linear regression with four valid data had the highest accuracy, with an RMSE of 1.52 K, with two valid data having the lowest accuracy, and with an RMSE in the range of 1.75–2.36 K, and the regression with three valid data had a relatively high accuracy, with an RMSE in the range of 1.53–1.84 K.

The validation results of cloudy-sky Ts reconstructed by TDCM, LCM, and ETGRM methods were displayed in Fig. 16. The comparison of the estimated dmTs with the ground-measured Ts from 2011 to 2020 at the 478 validation

TABLE III
TIME CONSUMPTION OF THE METHODS USED IN THIS STUDY

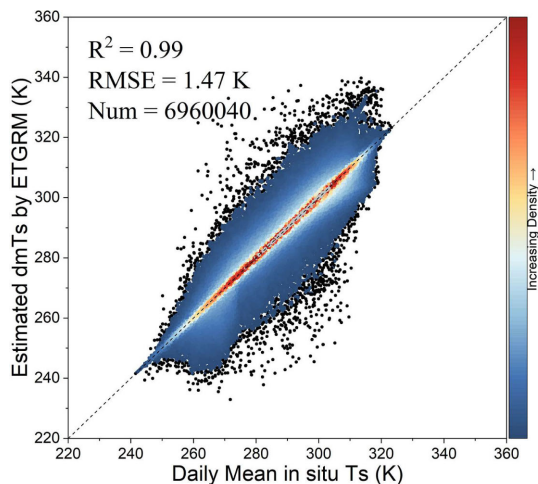| Condition	Method	PC configuration	Number of pixels/image	Runtime/image
clear-sky	MLR			73.41s
	LCM	16GB RAM, 64-bit operating system	9079685	64.55s
cloudy-sky	TDCM			45.51s
	ETGRM			90.05s

Fig. 13. Scatterplot of dmTs estimated by ETGRM versus in situ Ts at 1910 meteorological stations from 2011 to 2020. The gray diagonal lines are 1:1 lines.

sites shows that the TDCM estimated dmTs has the highest accuracy, with an R^2 of 0.94 and an RMSE of 2.73 K, and the LCM estimated results are second only to the TDCM, with an R^2 of 0.93 and an RMSE of 3.01 K. The Ts obtained from the ETGRM estimate at the validation sites performed relatively poorly with an R^2 of 0.87 and an RMSE of 4.69 K. However, ETGRM fits well at 1910 sites, probably due to the high number of missing MODIS dmTs data, especially in the southern region of China, where the only Ts data involved in the fitting within the sliding window are the in situ data, resulting in a high degree of agreement between the fitting results and the in situ Ts.

Fig. 17 illustrates the histograms of R^2 and RMSE for estimating cloud-sky dmTs at 478 validation sites using TDCM, LCM, and ETGRM. For LCM, validated against the measured dmTs data, 73.8% of them have R^2 greater than 0.9 and 13.4% of them have RMSE less than 2 K. Although the dmTs reconstructed by ETGRM can reach an overall R^2 of 0.87, the sites with R^2 greater than 0.9 account for only 1.35% of the validation sites and only 7.1% of them have RMSE less than 2 K, while for the dmTs constructed using TDCM, 78.5% of the sites have R^2 greater than 0.9 out of 478 sites, and 56.7% of the sites have RMSE values smaller than 2 K. The validation results show that the cloudy-sky dmTs data obtained with TDCM are in high agreement with the in situ dmTs, and the errors are more satisfying to the application requirements. Therefore, TDCM is finally adopted in this study to populate the MODIS dmTs under cloud sky from 2011 to 2020.
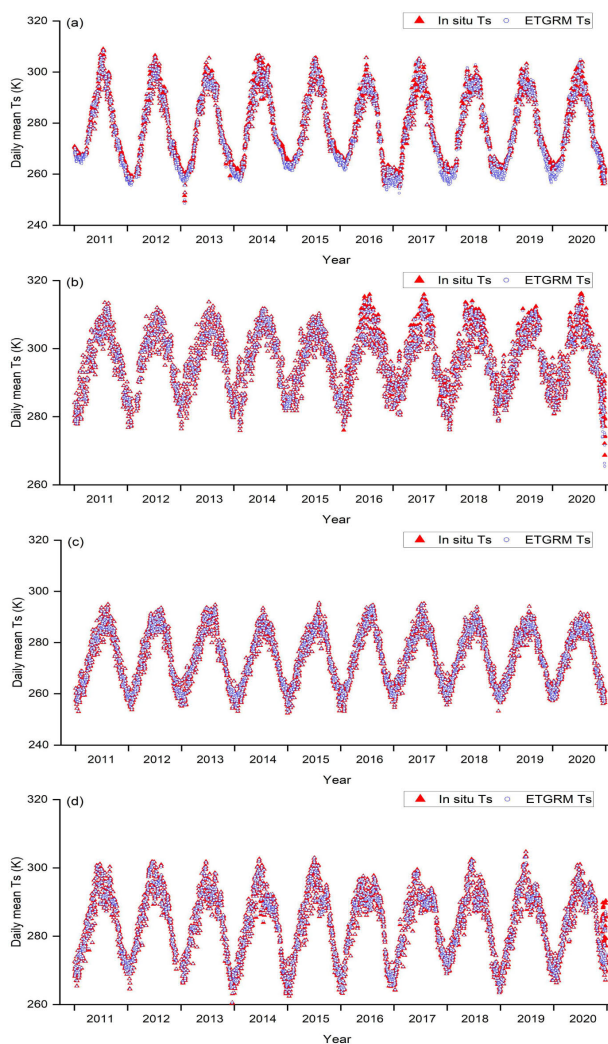

Fig. 14. In situ daily mean Ts and daily mean Ts estimated by ETGRM from 2011 to 2020 of the four randomly selected sites. (a) 50137, (b) 55680, (c) 56004, and (d) 59090.

D. Time Efficiency

Time efficiency is one of the issues that must be considered when conducting research on a large regional or even global scale. In this study, the limited computational resources are fully taken into account, and methods that are time-consuming and require a lot of computational power are discarded in the process of all-weather dmTs reconstruction, such as deep learning that requires GPUs or energy balancing methods that require multiple auxiliary variables.

Table III summarizes the device used in this study and the runtime of each method. Without considering the time spent on
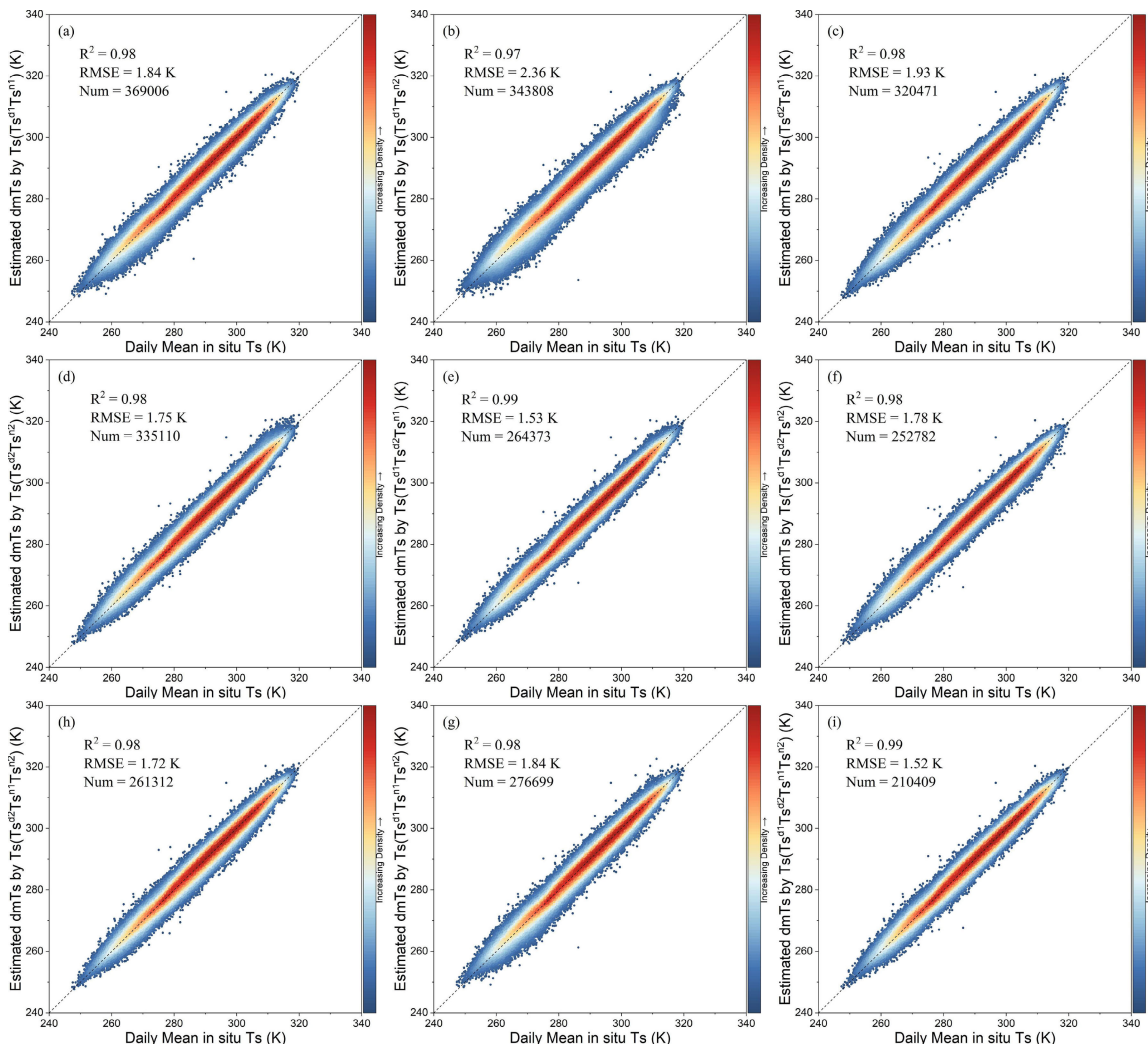
Fig. 15. Scatter plots of daily mean in situ Ts versus daily mean Ts estimated with multiple linear regression using (1)–(3) at 478 meteorological stations from 2011 to 2020. The gray diagonal lines are 1:1 lines. (a)–(i) dmTs estimated with the combinations of $Ts^{d1}\_Ts^{n1}$, $Ts^{d1}\_Ts^{n2}$, $Ts^{d2}\_Ts^{n1}$, $Ts^{d2}\_Ts^{n2}$, $Ts^{d1}\_Ts^{d2}\_Ts^{n1}$, $Ts^{d1}\_Ts^{d2}\_Ts^{n2}$, $Ts^{d1}\_Ts^{n1}\_Ts^{n2}$, $Ts^{d2}\_Ts^{n1}\_Ts^{n2}$, and $Ts^{d1}\_Ts^{d2}\_Ts^{n1}\_Ts^{n2}$ versus in situ dmTs.
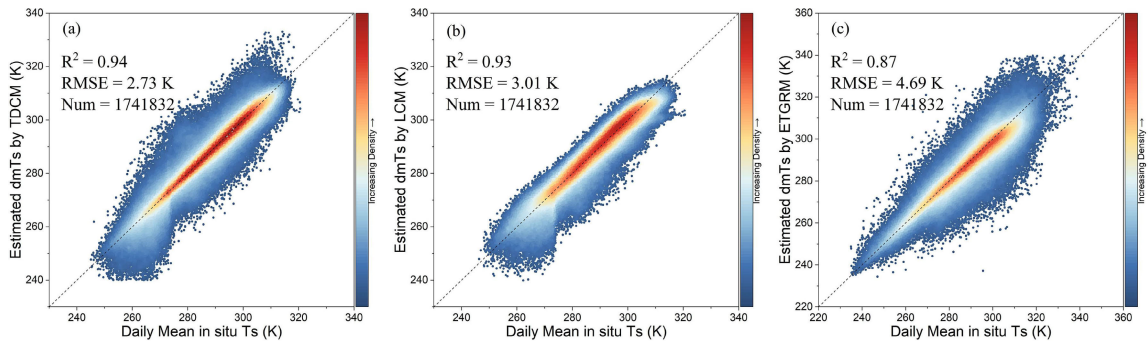

Fig. 16. Scatter plots of daily mean in situ Ts versus daily mean Ts reconstructed by (a) TDCM, (b) LCM, and (c) ETGRM methods at 478 sites from 2011 to 2020. The gray diagonal lines are 1:1 lines.

data preparation, the MLR + TDCM method used in this study takes less than 2 min to reconstruct one-day 1-km all-weather dmTs data for China region with the ordinary computational equipment. This proves the applicability of our method for reconstructing high-resolution temperatures on a large scale.

E. Spatio-Temporal Variation of Filled dmTs

Fig. 18 characterizes the spatial distribution and temporal variation of the reconstructed Ts from 2011 to 2020. Fig. 18(a)

shows the mean value of the multiyear average dmTs, which varies between 255 and 304 K, with a mean value of 284.8 K. Spatially, dmTs shows a latitudinal gradient characteristic, i.e., higher dmTs values at low latitudes and lower dmTs values at high latitudes. On the other hand, it is not difficult to find that the spatial distribution of dmTs is also affected by the surface elevation, which is manifested by the fact that the average dmTs in the Tibetan Plateau region is significantly lower than that in other regions. Fig. 18(c) shows the dynamic change of
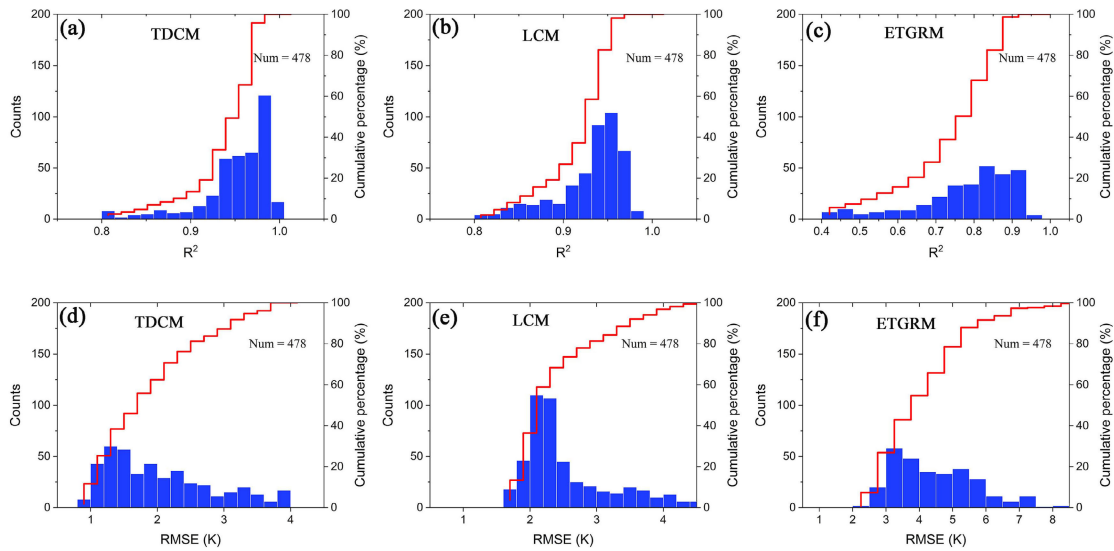
Fig. 17. Histograms of the R^2 and RMSE of the 478 validation sites to estimate the dmTs under cloudy-sky condition via (a) and (d) LCM, (b) and (e) TDCM, and (c) and (f) ETGRM.
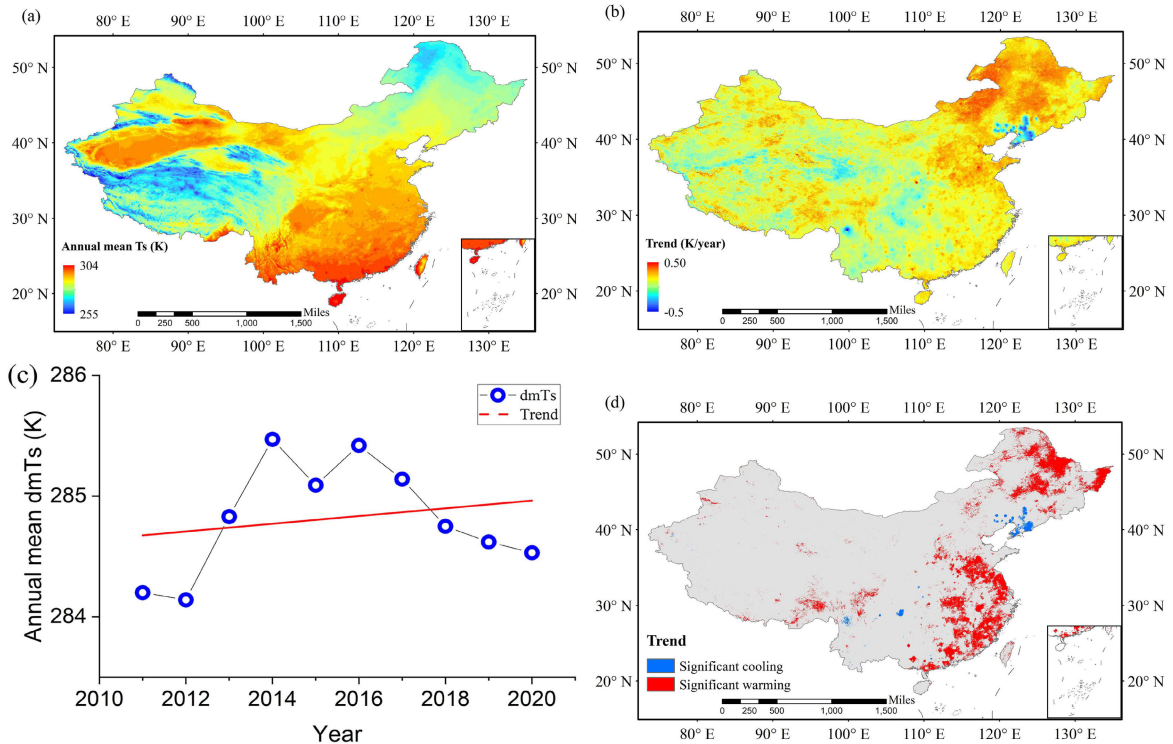

Fig. 18. Spatio-temporal variation of filled dmTs: (a) multiyear mean dmTs, (b) interannual change trend of dmTs, (c) annual mean dmTs, and (d) significant change trend.

the mean Ts of each year. As shown in the figure, the annual mean dmTs shows a fast warming trend from 2012 to 2014 and then fluctuates and decreases after that. However, the overall trend is still warming over the ten-year period.

Fig. 18(b) shows the trend of reconstructed dmTs during 2011–2020. In general, the change slope of dmTs varies from −0.5 to 0.5 K/year from 2011 to 2020, with an average change slope of 0.02 K/year. The share of warming regions is 59.06%, which is much larger than the share of cooling regions, which is 40.92%. Of these, 12.40% passed the significance level ($p < 0.05$), with 11.49% significantly warming and 0.91%

significantly cooling. The average slope of the significantly changed areas is 0.12 K/year. The significant warming slope is 0.15 K/year and the significant cooling slope is −0.27 K/year. The spatial distribution of the significant change areas is shown in Fig. 18(d).

V. DISCUSSION

A. Reconstruction of dmTs

The estimation of MODIS clear-sky dmTs by the multiple linear regression method is to obtain the relationship between

satellite instantaneous Ts and daily average Ts by constructing the relationship between the in situ instantaneous Ts data and daily average Ts, thus obtaining the MODIS dmTs with more data that are closer to the in situ data from the ground stations. It has been shown that the accuracy of dmTs reconstructed by multiple linear regression is higher than that of dmTs obtained by averaging the instantaneous Ts [47].

The reconstruction of the cloudy-sky data combines 1910 ground-based observations, and the reconstruction accuracy of TDCM is higher than the other two methods. In this case, the LCM is a point-to-point correction of the ERA5-land Ts data by using ground-based observations, but the point-by-point fitting uses the same set of correction coefficients for the corresponding location of each observation site over the period of 2011–2020 and thus suffers from a large error. The TDCM, on the other hand, obtains the daily TD between the MODIS dmTs and ERA5-land Ts and adds the ground-based observations to improve the accuracy, so the TDCM filling result is slightly better. ETGRM fills cloudy-sky Ts by constructing gradient variations relationship between temperature and elevation, and its filling accuracy performs well at the experimental sites (1910 sites) but poorly at the validation sites due to the high level of missing MODIS dmTs data; even the ground-based observations are added. Within the set sliding window, the fitting coefficients are mostly dependent on the limit site data and very few satellite data, so the performance is excellent at 1910 sites, but the results of the fitting are highly biased at the locations where no site exists or where there are many missing data. Furthermore, in order to save time and cost, the sliding direction of the sliding window in this study was only set in the latitude direction, which could potentially improve the filling accuracy of the method if the sliding window fitting in the longitude direction is added.

We further discuss the differences in the spatial distribution of the accuracy of dmTs reconstructed by the TDCM method. Fig. 19(a) and (b) shows the spatial distribution of the accuracy indicators R^2 and RMSE for the dmTs filled by the TDCM method. As shown in the figure, the western part of China, especially the Tibetan Plateau region, has an overall R^2 below 0.8 and RMSEs mostly above 3 K. The overall accuracy is significantly lower than that in the eastern and southern parts of the study area. The higher altitude and the smaller number of ground-based observation stations are the main factors contributing to the lower accuracy of the filled dmTs in this region. However, from the average number of sunny days over the years presented in Fig. 19(c), it can be seen that the number of sunny days in the northwest region is above 200 days per year, with a maximum of 310 days. Therefore, the dmTs data in this region are mainly derived from the MODIS Ts data, which means that the poor performance of the TDCM method in this region does not affect the quality of the final data.

B. Changing Trends in dmTs

The results of the study showed that dmTs showed a significant warming trend during 2011–2020, which coincided with the significant warming mentioned in the report of the
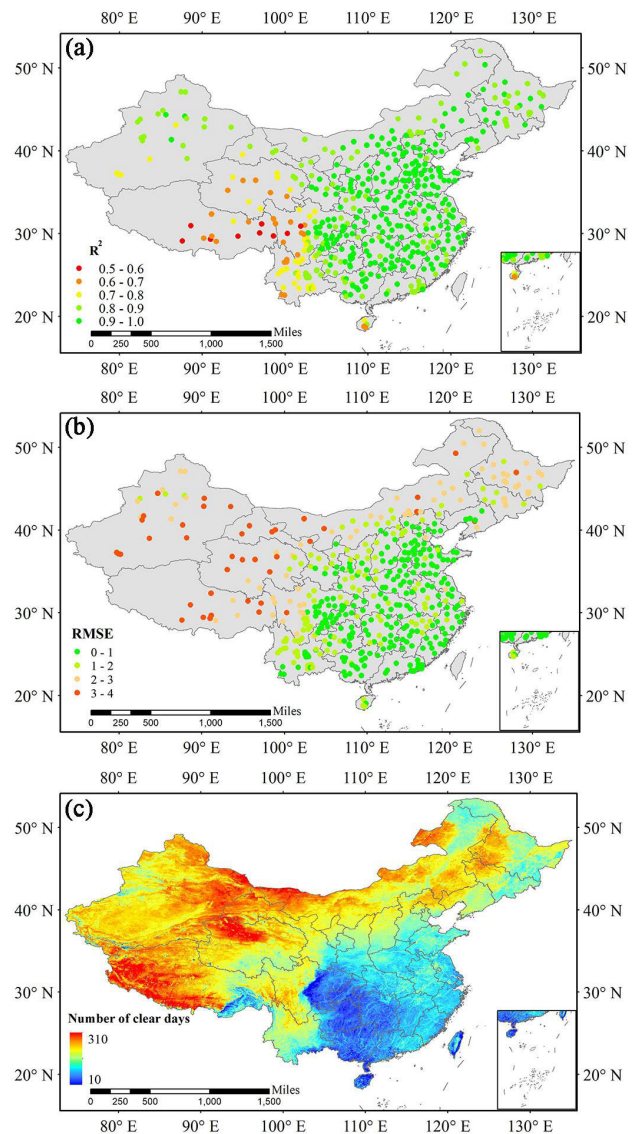

Fig. 19. Spatial distribution of (a) R^2 of TDCM method, (b) RMSE of TDCM method, and (c) multiyear mean number of clear days.
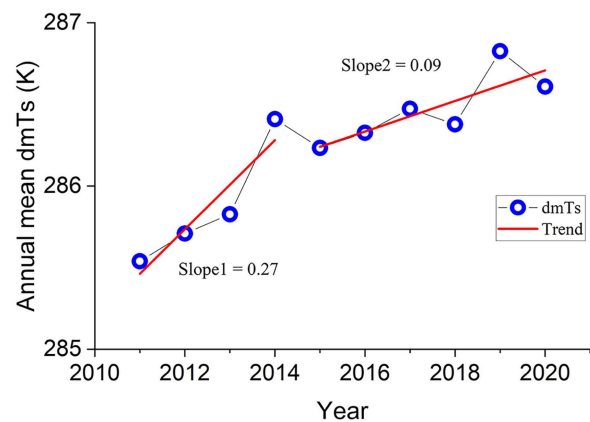

Fig. 20. Dynamics of annual mean dmTs within the significant change zone.

Intergovernmental Panel on Climate Change [60]. However, in some previous studies, it has been shown that a significant cooling trend was observed in some parts of China up to 2018,

especially in the northeastern plains and southern regions [7], [25]. The reason for this opposite result is, on the one hand, due to the different lengths of the time series of the research data. The present study only analyzes the dmTs for the years 2011–2020, which is a shorter time series. As can be seen in Fig. 18(c), the annual mean dmTs turned around in 2014, also with a cooling trend, but still on a warming trend over the whole study period.

In addition, we further analyzed the annual mean dmTs in the region where the significant change occurred, as shown in Fig. 20. Within the significant change region, the annual mean dmTs also changed over 2014, with the slope of change decreasing from 0.27 to 0.09, but still with a warming trend. On the other hand, the different spatial and temporal resolutions of the study data, as well as the differences in the number of ground-based observation stations used, also affect the results of the study [61], [62]. Comparative validation after conversion to the same spatial and temporal resolution and time series length would be more convincing, and it will be further improved in future studies.

VI. Conclusion

For the reconstruction of all-weather 1-km dmTs data, most previous studies have filled most of the missing Ts data by fusion with passive microwave Ts products. However, the spatial resolution of passive microwave products is low and the inter-orbit gaps remain unresolved. Therefore, in recent years, reanalysis data with its advantage of spatial integrity have gradually become an important aid in acquiring high-resolution all-weather Ts data. In addition, another advantage of this study is the 2388 meteorological stations with a time-continuous and high precision hourly/daily Ts datasets, which were selected from nearly 10 000 stations. The reliability of ground-based observations of Ts is unquestionable.

Thus, the results of this study suggest that the multiple linear regression method performs well in reconstructing MODIS clear-sky Ts data with R^2 ranging from 0.97 to 0.99 and RMSE ranging from 1.52 to 2.36 K validated with in situ data. For the cloudy sky, the comparison of three methods shows that the ERA5-land dmTs corrected by TD has the best agreement with the in situ validation Ts data, with the value of R^2 being 0.94 and RMSE being 2.73 K, which also indicated that the accuracy of reconstructed dmTs is plausible. In addition, the time efficiency of the methodology used in this study is high.

In detail, the desirable features of the dmTs reconstruction strategy adopted in this study are as follows. First, a large number of measured Ts data from ground stations are added to improve the reconstruction accuracy of the all-weather Ts so that the reconstructed data are closer to the real surface state. Second, the corrected daily ERA5-land dmTs data are used to fill the missing data of the cloud sky without adding other auxiliary data (e.g., vegetation, elevation, and radiation), which avoids the uncertainty of the results that is increased by the uncertainty of multiple auxiliary variables themselves and their uncertain relationships with Ts. Finally, the all-weather dmTs reconstruction strategy adopted in this study acquires a high spatial and temporal resolution and high accuracy Ts dataset

with a fast speed, which not only describes the change of surface thermal state more exhaustively and accurately but also reduces the computational cost dramatically compared with other eight-day or monthly Ts datasets.

In this study, we aim to obtain MODIS all-weather daily mean surface temperatures accurately and quickly by using multisource data. Although the results of filling were satisfactory in both clear sky and cloudy sky, some limitations remain. First, in the clear-sky case, we discarded the cases where only one moment or only daytime or only nighttime valid observations existed, which wastes a lot of valid data. Therefore, how to fully utilize the instantaneous Ts data in the above cases and increase the amount of reconstructed dmTs data while guaranteeing the accuracy is a problem to be solved in the next work. Furthermore, in order to reduce the computational burden, the hour-by-hour in situ Ts data are used in constructing the relationship between the instantaneous Ts and the dmTs, and it is assumed that the temperature varies linearly in the adjacent time, which will increase the uncertainty of the results to a certain extent. Therefore, the utilization of the minute-by-minute in situ Ts data from the meteorological observation stations will obtain superior results.
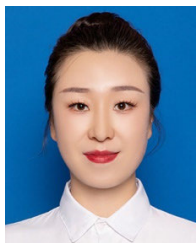
Despite some limitations, the all-weather 1-km daily mean MODIS Ts data obtained in this study for the Chinese region from 2011 to 2020 not only ensure the completeness of the data but also better represent the dynamics of the real thermal state of the land surface, which is helpful for real-time capture of weather extremes and meteorological hazards such as droughts and heat waves.

References

[1] Z. Zeng et al., "Climate mitigation from vegetation biophysical feedbacks during the past three decades," *Nature Climate Change*, vol. 7, no. 6, pp. 432–436, Jun. 2017, doi: 10.1038/nclimate3299.

[2] X. Liu, Y. Zhou, W. Yue, X. Li, Y. Liu, and D. Lu, "Spatiotemporal patterns of summer urban heat island in Beijing, China using an improved Land Surface Temperature," *J. Cleaner Prod.*, vol. 257, Jun. 2020, Art. no. 120529, doi: 10.1016/j.jclepro.2020.120529.

[3] E. Erlat, M. Türkeş, and H. Güler, "Analysis of long-term trends and variations in extreme high air temperatures in may over Turkey and a record-breaking heatwave event of May 2020," *Int. J. Climatol.*, vol. 42, no. 16, pp. 9319–9343, Dec. 2022, doi: 10.1002/joc.7821.

[4] Z. Li et al., "Satellite remote sensing of global Land Surface Temperature: Definition, methods, products, and applications," *Rev. Geophys.*, vol. 61, no. 1, Mar. 2023, Art. no. e2022RG000777, doi: 10.1029/2022rg000777.

[5] Y. Mo, Y. Xu, Y. Liu, Y. Xin, and S. Zhu, "Comparison of gap-filling methods for producing all-weather daily remotely sensed near-surface air temperature," *Remote Sens. Environ.*, vol. 296, Oct. 2023, Art. no. 113732, doi: 10.1016/j.rse.2023.113732.

[6] J. Hooker, G. Duveiller, and A. Cescatti, "A global dataset of air temperature derived from satellite remote sensing and weather stations," *Sci. Data*, vol. 5, no. 1, Nov. 2018, Art. no. 1, doi: 10.1038/sdata.2018.246.

[7] B. Zhao et al., "A combined Terra and Aqua MODIS Land Surface Temperature and meteorological station data product for China from 2003 to 2017," *Earth Syst. Sci. Data*, vol. 12, no. 4, pp. 2555–2577, Oct. 2020, doi: 10.5194/essd-12-2555-2020.

[8] J. Qin et al., "Temporally extended satellite-derived surface air temperatures reveal a complete warming picture on the Tibetan Plateau," *Remote Sens. Environ.*, vol. 285, Feb. 2023, Art. no. 113410, doi: 10.1016/j.rse.2022.113410.

[9] R. Yao et al., "Global seamless and high-resolution temperature dataset (GSHTD), 2001–2020," *Remote Sens. Environ.*, vol. 286, Mar. 2023, Art. no. 113422, doi: 10.1016/j.rse.2022.113422.

[10] C. Beale et al., "Comparison of diurnal variation of Land Surface Temperature from GOES-16 ABI and MODIS instruments," *IEEE Geosci. Remote Sens. Lett.*, vol. 17, no. 4, pp. 572–576, Apr. 2020, doi: 10.1109/LGRS.2019.2930174.

[11] M. Amraoui, C. C. DaCamara, and J. M. C. Pereira, "Detection and monitoring of African vegetation fires using MSG-SEVIRI imagery," *Remote Sens. Environ.*, vol. 114, no. 5, pp. 1038–1052, May 2010, doi: 10.1016/j.rse.2009.12.019.

[12] S. Zhou and J. Cheng, "An improved temperature and emissivity separation algorithm for the advanced Himawari imager," *IEEE Trans. Geosci. Remote Sens.*, vol. 58, no. 10, pp. 7105–7124, Oct. 2020, doi: 10.1109/TGRS.2020.2979846.

[13] S. Dong, J. Cheng, J. Shi, C. Shi, S. Sun, and W. Liu, "A data fusion method for generating hourly seamless Land Surface Temperature from Himawari-8 AHI data," *Remote Sens.*, vol. 14, no. 20, p. 5170, Oct. 2022, doi: 10.3390/rs14205170.

[14] D. Hu, L. Yang, J. Zhou, and L. Deng, "Estimation of urban energy heat flux and anthropogenic heat discharge using aster image and meteorological data: Case study in Beijing metropolitan area," *J. Appl. Remote Sens.*, vol. 6, no. 1, Sep. 2012, Art. no. 063559, doi: 10.1117/1.jrs.6.063559.

[15] M. Abrams et al., "The Advanced Spaceborne Thermal Emission and Reflection Radiometer (ASTER) after fifteen years: Review of global products," *Int. J. Appl. Earth Observ. Geoinf.*, vol. 38, pp. 292–301, Jun. 2015, doi: 10.1016/j.jag.2015.01.013.

[16] X. Liu, B.-H. Tang, G. Yan, Li, and Z.-L. Liang, "Retrieval of global orbit drift corrected land surface temperature from long-term AVHRR data," *Remote Sens.*, vol. 11, no. 23, p. 2843, Nov. 2019, doi: 10.3390/rs11232843.

[17] Z. Wan, "New refinements and validation of the collection-6 MODIS land-surface temperature/emissivity product," *Remote Sens. Environ.*, vol. 140, pp. 36–45, Jan. 2014, doi: 10.1016/j.rse.2013.08.027.

[18] Z. L. Li et al., *Satellite-Derived Land Surface Temperature: Current Status and Perspectives*, no. 131. Amsterdam, The Netherlands: Elsevier, 2013, doi: 10.1016/J.RSE.2012.12.008.

[19] X. Li, Y. Zhou, G. R. Asrar, and Z. Zhu, "Creating a seamless 1 km resolution daily Land Surface Temperature dataset for urban and surrounding areas in the conterminous United States," *Remote Sens. Environ.*, vol. 206, pp. 84–97, Mar. 2018, doi: 10.1016/j.rse.2017.12.010.

[20] X. Li, Y. Zhou, G. R. Asrar, and Z. Zhu, "Developing a 1 km resolution daily air temperature dataset for urban and surrounding areas in the conterminous United States," *Remote Sens. Environ.*, vol. 215, pp. 74–84, Sep. 2018, doi: 10.1016/j.rse.2018.05.034.

[21] A. F. Militino, M. D. Ugarte, and M. Montesino, "Filling missing data and smoothing altered data in satellite imagery with a spatial functional procedure," *Stochastic Environ. Res. Risk Assessment*, vol. 33, no. 10, pp. 1737–1750, Oct. 2019, doi: 10.1007/s00477-019-01711-0.

[22] S.-B. Duan, Z.-L. Li, N. Wang, H. Wu, and B.-H. Tang, "Evaluation of six land-surface diurnal temperature cycle models using clear-sky in situ and satellite data," *Remote Sens. Environ.*, vol. 124, pp. 15–25, Sep. 2012, doi: 10.1016/j.rse.2012.04.016.

[23] P. Fu and Q. Weng, "Consistent Land Surface Temperature data generation from irregularly spaced landsat imagery," *Remote Sens. Environ.*, vol. 184, pp. 175–187, Oct. 2016, doi: 10.1016/j.rse.2016.06.019.

[24] W. Zhao, J. He, G. Yin, F. Wen, and H. Wu, "Spatiotemporal variability in Land Surface Temperature over the mountainous region affected by the 2008 Wenchuan earthquake from 2000 to 2017," *J. Geophys. Res., Atmos.*, vol. 124, no. 4, pp. 1975–1991, Feb. 2019, doi: 10.1029/2018jd030007.

[25] Y. Yu et al., "Interannual spatiotemporal variations of Land Surface Temperature in China from 2003 to 2018," *IEEE J. Sel. Topics Appl. Earth Observ. Remote Sens.*, vol. 14, pp. 1783–1795, 2021, doi: 10.1109/JSTARS.2020.3048823.

[26] Y. Xu and Y. Shen, "Reconstruction of the land surface temperature time series using harmonic analysis," *Comput. Geosci.*, vol. 61, pp. 126–132, Dec. 2013, doi: 10.1016/j.cageo.2013.08.009.

[27] Z. Pan, Y. Hu, and B. Cao, "Construction of smooth daily remote sensing time series data: A higher spatiotemporal resolution perspective," *Open Geospatial Data, Softw. Standards*, vol. 2, no. 1, p. 25, Oct. 2017, doi: 10.1186/s40965-017-0038-z.

[28] W. U. Di, C. Jian, S. Man, Q. Bangyong, and L. I. Shengyang, "Reconstruction of land surface temperature time-series datasets of FY-2F based on Savitzky-Golay filter," *Remote Sens. Land Resour.*, vol. 31, pp. 59–65, Jan. 2019. Accessed: Dec. 15, 2023. [Online]. Available: http://en.cnki.com.cn/Article_en/CJFDTotal-GTYG201902009.htm

[29] P. Fracas and E. Zondervan, "Fast Fourier transforms for micro-grid climate computing," *Comput. Aided Chem. Eng.*, vol. 46, pp. 1657–1662, Jul. 2019, doi: 10.1016/B978-0-12-818634-3.50277-0.

[30] E. Ozelkan, S. Bagis, B. Berk Ustundag, E. C. Ozelkan, M. Yucel, and C. Ormeci, "Land Surface Temperature–based spatial interpolation using a modified inverse distance weighting method," in *Proc. 2nd Int. Conf. Agro-Geoinformatics (Agro-Geoinformatics)*, Aug. 2013, pp. 110–115, doi: 10.1109/Argo-Geoinformatics.2013.6621890.

[31] J. Tan et al., "Coupling random forest and inverse distance weighting to generate climate surfaces of precipitation and temperature with multiple-covariates," *J. Hydrol.*, vol. 598, Jul. 2021, Art. no. 126270, doi: 10.1016/j.jhydrol.2021.126270.

[32] A. Shtiliyanova, G. Bellocchi, D. Borras, U. Eza, R. Martin, and P. Carrère, "Kriging-based approach to predict missing air temperature data," *Comput. Electron. Agricult.*, vol. 142, pp. 440–449, Nov. 2017, doi: 10.1016/j.compag.2017.09.033.

[33] S. Bhattacharjee, J. Chen, and S. K. Ghosh, "Spatio-temporal prediction of Land Surface Temperature using semantic kriging," *Trans. GIS*, vol. 24, no. 1, pp. 189–212, Jan. 2020, doi: 10.1111/tgis.12596.

[34] T. Hengl, G. B. M. Heuvelink, M. P. Tadić, and E. J. Pebesma, "Spatio-temporal prediction of daily temperatures using time-series of MODIS LST images," *Theor. Appl. Climatol.*, vol. 107, nos. 1–2, pp. 265–277, Jan. 2012, doi: 10.1007/s00704-011-0464-2.

[35] D. J. Weiss, P. M. Atkinson, S. Bhatt, B. Mappin, S. I. Hay, and P. W. Gething, "An effective approach for gap-filling continental scale remotely sensed time-series," *ISPRS J. Photogramm. Remote Sens.*, vol. 98, pp. 106–118, Dec. 2014, doi: 10.1016/j.isprsjprs.2014.10.001.

[36] L. Sun et al., "Reconstructing daily clear-sky land surface temperature for cloudy regions from MODIS data," *Comput. Geosci.*, vol. 105, pp. 10–20, Aug. 2017, doi: 10.1016/j.cageo.2017.04.007.

[37] D. Long et al., "Generation of MODIS-like land surface temperatures under all-weather conditions based on a data fusion approach," *Remote Sens. Environ.*, vol. 246, Sep. 2020, Art. no. 111863, doi: 10.1016/j.rse.2020.111863.

[38] W. Zhao and S.-B. Duan, "Reconstruction of daytime land surface temperatures under cloud-covered conditions using integrated MODIS/Terra land products and MSG geostationary satellite data," *Remote Sens. Environ.*, vol. 247, Sep. 2020, Art. no. 111931, doi: 10.1016/j.rse.2020.111931.

[39] Y. Chen, Z. Nan, Z. Cao, M. Ou, and K. Feng, "A stepwise framework for interpolating Land Surface Temperature under cloudy conditions based on the solar-cloud-satellite geometry," *ISPRS J. Photogramm. Remote Sens.*, vol. 197, pp. 292–308, Mar. 2023, doi: 10.1016/j.isprsjprs.2023.02.004.

[40] C. André, C. Ottlé, A. Royer, and F. Maignan, "Land Surface Temperature retrieval over circumpolar Arctic using SSM/I–SSMIS and MODIS data," *Remote Sens. Environ.*, vol. 162, pp. 1–10, Jun. 2015, doi: 10.1016/j.rse.2015.01.028.

[41] D. Zhou et al., "Croplands intensify regional and global warming according to satellite observations," *Remote Sens. Environ.*, vol. 264, Oct. 2021, Art. no. 112585, doi: 10.1016/j.rse.2021.112585.

[42] S.-B. Duan, Z.-L. Li, and P. Leng, "A framework for the retrieval of all-weather land surface temperature at a high spatial resolution from polar-orbiting thermal infrared and passive microwave data," *Remote Sens. Environ.*, vol. 195, pp. 107–117, Jun. 2017, doi: 10.1016/j.rse.2017.04.008.

[43] P. Hou, Y. Chen, W. Qiao, G. Cao, W. Jiang, and J. Li, "Near-surface air temperature retrieval from satellite images and influence by wetlands in urban region," *Theor. Appl. Climatol.*, vol. 111, nos. 1–2, pp. 109–118, Jan. 2013, doi: 10.1007/s00704-012-0629-7.

[44] A. Jia, H. Ma, S. Liang, and D. Wang, "Cloudy-sky Land Surface Temperature from VIIRS and MODIS satellite data using a surface energy balance-based method," *Remote Sens. Environ.*, vol. 263, Sep. 2021, Art. no. 112566, doi: 10.1016/j.rse.2021.112566.

[45] H. Hersbach et al., "The ERA5 global reanalysis," *Quart. J. Roy. Meteorolog. Soc.*, vol. 146, no. 730, pp. 1999–2049, Jul. 2020, doi: 10.1002/qj.3803.

[46] R. Gelaro et al., "The modern-era retrospective analysis for research and applications, version 2 (MERRA-2)," *J. Climate*, vol. 30, no. 14, pp. 5419–5454, Jul. 2017, doi: 10.1175/jcli-d-16-0758.1.

[47] Z. Xing et al., "Estimation of daily mean land surface temperature at global scale using pairs of daytime and nighttime MODIS instantaneous observations," *ISPRS J. Photogramm. Remote Sens.*, vol. 178, pp. 51–67, Aug. 2021, doi: 10.1016/j.isprsjprs.2021.05.017.

[48] X. Kou, L. Jiang, Y. Bo, S. Yan, and L. Chai, "Estimation of Land Surface Temperature through blending MODIS and AMSR-E data with the Bayesian maximum entropy method," *Remote Sens.*, vol. 8, no. 2, p. 105, Jan. 2016, doi: 10.3390/rs8020105.

[49] A. Sekulić, M. Kilibarda, G. B. M. Heuvelink, M. Nikolić, and B. Bajat, "Random forest spatial interpolation," *Remote Sens.*, vol. 12, no. 10, p. 1687, May 2020, doi: 10.3390/rs12101687.

[50] C. Yoo, J. Im, D. Cho, N. Yokoya, J. Xia, and B. Bechtel, "Estimation of all-weather 1 km MODIS land surface temperature for humid summer days," *Remote Sens.*, vol. 12, no. 9, p. 1398, Apr. 2020, doi: 10.3390/rs12091398.

[51] X. Zhang, J. Zhou, F.-M. Göttsche, W. Zhan, S. Liu, and R. Cao, "A method based on temporal component decomposition for estimating 1-km all-weather Land Surface Temperature by merging satellite thermal infrared and passive microwave observations," *IEEE Trans. Geosci. Remote Sens.*, vol. 57, no. 7, pp. 4670–4691, Jul. 2019, doi: 10.1109/TGRS.2019.2892417.

[52] Z. Wan and Z.-L. Li, "MODIS Land Surface Temperature and emissivity," in *Land Remote Sensing and Global Environmental Change: NASA's Earth Observing System and the Science of ASTER and MODIS* (Remote Sensing and Digital Image Processing), B. Ramachandran, C. O. Justice, and M. J. Abrams, Eds. New York, NY, USA: Springer, 2011, pp. 563–577, doi: 10.1007/978-1-4419-6749-7_25.

[53] J. Mu noz-Sabater et al., "ERA5-Land: A state-of-the-art global reanalysis dataset for land applications," *Earth Syst. Sci. Data*, vol. 13, no. 9, pp. 4349–4383, Sep. 2021, doi: 10.5194/essd-13-4349-2021.

[54] X. Liu et al., "Local temperature responses to actual land cover changes present significant latitudinal variability and asymmetry," *Sci. Bull.*, vol. 68, no. 22, pp. 2849–2861, Nov. 2023, doi: 10.1016/j.scib.2023.09.046.

[55] Z. Li, "An enhanced dual IDW method for high-quality geospatial interpolation," *Sci. Rep.*, vol. 11, no. 1, p. 9903, May 2021, doi: 10.1038/s41598-021-89172-w.

[56] H. B. Mann, "Nonparametric test against trend," *Econometrica*, vol. 13, pp. 245–259, Jul. 1945, doi: 10.2307/1907187.

[57] M. Hussain and I. Mahmud, "pyMannKendall: A Python package for non parametric Mann Kendall family of trend tests," *J. Open Source Softw.*, vol. 4, no. 39, p. 1556, Jul. 2019, doi: 10.21105/joss.01556.

[58] H. Theil, "A rank-invariant method of linear and polynomial regression analysis," *Nederl. Akad. Wetensch. Proc.*, vol. 12, no. 2, pp. 345–381, 1992, doi: 10.1007/978-94-011-2546-8_20.

[59] P. K. Sen, "Estimates of the regression coefficient based on Kendall's tau," *J. Amer. Stat. Assoc.*, vol. 63, no. 324, pp. 1379–1389, 1968, doi: 10.1080/01621459.1968.10480934.

[60] W. G. I. Ofipcc, "Climate change 2013: The physical science basis," *Contrib. Work.*, vol. 43, no. 22, pp. 866–871, 2013, doi: 10.1007/BF00524943.

[61] L. He et al., "Non-symmetric responses of leaf onset date to natural warming and cooling in northern ecosystems," *PNAS Nexus*, vol. 2, no. 9, Sep. 2023, Art. no. pgad308, doi: 10.1093/pnasnexus/pgad308.

[62] Y. Li et al., "Biophysical impacts of Earth greening can substantially mitigate regional Land Surface Temperature warming," *Nature Commun.*, vol. 14, no. 1, pp. 1–12, Jan. 2023, doi: 10.1038/s41467-023-35799-4.

Shibo Fang is currently a Professor with the Chinese Academy of Meteorological Sciences (CAMS), China Meteorological Administration (CMA), Beijing, China. He was a Visiting Professor with Florida Climate Institute, University of Florida, Gainesville, FL, USA, from 2013 to 2014. He is leading the Remote Sensing and Agrometeorology Team at CMA. He is well known for his agriculture remote sensing and agriculture response to climate change expertise, organizational ability, and program leadership. In the last ten years, he worked on agriculture remote sensing and mainly focused on developing satellite remote sensing tools to get the land surface soil moisture to monitor the drought and water-logging stresses and disasters of terrestrial ecosystem. He collaborates in several international studies, such as funds of U.K. STFC Newton Fund and China NSFC, U.K. Newton Fund, and NSFC China—ISTP Canada, focused on improving and inter-comparing agricultural tools for crops health and agrometeorological disasters.

Wen Zhuo received the B.S. degree in geographic information system from Huazhong Agricultural University, Wuhan, China, in 2013, and the M.S. degree in geographic information system and the Ph.D. degree in agricultural information technology from China Agricultural University, Beijing, China, in 2015 and 2020, respectively.

He is currently a Post-Doctoral Fellow with the Chinese Academy of Meteorological Sciences, Beijing. His research interests include remote sensing data assimilation with crop growth models, drought monitoring, and climate change impacts on agriculture using remote sensing.

Yanru Yu received the B.S. and M.S. degrees from Hebei GEO University, Shijiazhuang, China, in 2014 and 2018, respectively, and the Ph.D. degree from the Chinese Academy of Agricultural Sciences, Beijing, China, in 2022.

She is currently a Post-Doctoral Fellow with the Chinese Academy of Meteorological Sciences, Beijing. Her main research areas include long-term remote sensing data generation, climate change and causality analysis, and remote sensing monitoring of agricultural meteorological disasters.

Jiahao Han received the B.S. and M.S. degrees in applied meteorology from the Nanjing University of Information Science and Technology, Nanjing, China, in 2019 and 2022, respectively. He is currently pursuing the Ph.D. degree with the Chinese Academy of Meteorological Sciences. He has authored over ten journals and conference papers in the areas of remote sensing and meteorological disasters. His research interests include disaster remote sensing monitoring and machine learning.